Available online at www.sciencedirect.com
ScienceDirect
Applied Catalysis B: Environmental 82 (2008) 169–179
APPLIED CATALYSIS B: ENVIRONMENTAL
www.elsevier.com/locate/apcatb

Heterogeneous catalytic activity of NiO-silica composites designated with cubic *Pm3n* cage nanostructures

Sherif A. El-Safty *, Yoshimichi Kiyozumi, Takaaki Hanaoka, Fujio Mizukami

Research Center for Compact Chemical Process, National Institute of Advanced Industrial Science and Technology (AIST), 4-2-1, Nigatake, Miyagino-ku, Sendai 983-8551, Japan

Received 30 August 2007; accepted 24 January 2008
Available online 7 February 2008

Abstract

The fabrication of nanomaterials with the active network sites has led to efficient transport and easier diffusion of guest species in the catalytic application. In this regard, the NiO-supported cage monoliths show evidence to act as effective catalysts toward the oxidation of organic pollutants. Here, the cage-like NiO-silica catalyst with large particle size, cage-like pores, and ordered cubic *Pm3n* (HOM-9) structures could be fabricated by a simple, in short period (~5 min), and direct strategy in which microemulsion liquid crystalline phase of Brij 56 ($C_{16}EO_{10}$) surfactant was used as a template. Our synthetic strategy revealed that the nickel oxide nanoparticles were wrapped onto the pore surface matrices of the cubic *Pm3n* monoliths, indicating the simplicity and flexibility to control the geometry, morphology and dispersion of particles. No significant change in the cubic *Pm3n* (NiO/HOM-9) phase structures was evident by using this synthetic manipulation; however, high nickel contents up to Si/Ni ratios ~1 were added to the phase composition domains. Results from the analysis techniques including XRD, N_2 isotherms, TEM, XPS, and EDX revealed that the NiO nanoparticles with irregular sizes might be embedded, to some extent, into the pore cavity, particularly with low content of NiO. In turn, with low Si/Ni ratios, The NiO crystallite particles underwent the anisotropic growth to larger sizes (~15 nm) resulted from the aggregation effect, leading to the difficulty to be wrapped into the pore cavity. Practically important results were that the NiO-supported cage monoliths were used as effective catalysts for the oxidation of aminophenols in aqueous solution. However, among all NiO-supported amorphous and ordered silica materials, the NiO/HOM-9 catalyst with open, uniform pore-cage architectures, high surface area and large pore volumes allowed efficient adsorption and diffusion of aminophenols to the active site of NiO clusters, leading to high degree of conversion and reaction rate. On such heterogeneous catalytic systems, the reaction affinity of aminophenols was substantially affected by the structural feature of the catalysts, amount and degree of dispersion NiO particles onto the cubic cage pore surfaces, and the controlled temperature conditions.

Keywords: Monoliths; Cage pores; Organic pollutant; Oxidation reaction; NiO-supported catalysts

1. Introduction

Functional materials with regularly spaced nanometer-sized pores and three-dimensional geometries have attracted great interest in nanotechnology and science in the last decade [1–3]. Confinement properties of ordered mesoporous inorganic materials such as large surface area, regular connecting porosity with control sizes, shapes and volumes can lead to wide-spread applications in catalysis [4], adsorption [5], sensing [6], and electronics [7]. Since the discovery of MS41 materials, researchers have expanded the basic motif of using liquid crystals as structural imprints to cast the shape of the silica mesoporous materials [8]. The developments in the processing strategies of ordered mesoporous materials led to control over material compositions and structures. However, the surfactant moieties can be used to tune the formation of these mesoporous materials with various mesophases such as lamellar, hexagonal and cubic symmetries [9]. Design of transition metals and metal oxides in nanoscale architectures and ordered pore geometries is of particular interest in the synthesis of unique nanomaterials due to their variable oxidation states, and properties which often lead to tailored materials with unusual chemical and physical utilities [10–13]. In addition, metal oxides-emerged mesoporous silica materials have been reported with various pore structures, making them important materials with considerable and versatile properties [14].

* Corresponding author. Tel.: +81 22 237 5226; fax: +81 22 237 5226.
E-mail address: sherif.el-safty@aist.go.jp (S.A. El-Safty).

0926-3373/$ – see front matter
doi:10.1016/j.apcatb.2008.01.027

Several methods of the fabrication of nickel oxide-supported mesoporous silica materials have been developed in the past decade. Among these techniques, the impregnation, ion exchange, and direct incorporation and deposition of nickel precursors into the ordered mesoporous silica materials are the most common methods used [15–20]. However, limitations of using these approaches exist in the range of the amounts of the incorporated catalysts and the sophisticated procedures in terms of intensive, time-consuming and hydrothermal treatments. In addition, Zhao and co-workers have been reported one-step approach that is the most often manifest for tailoring not only the deposition of NiO ($\leq$30 wt%) but also several metal oxides into the large mesopores of hexagonal *P6mm* monolithic materials using liquid-paraffin-medium protected solvent evaporation for long gelation process (several hours) [21]. However, practical method is still being intensively required to control the pore geometry, dimension and regularity in an efficient and systematic methodology during the incorporation of the metal oxides into the nanostructured materials. Here, we reported successful fabrication of high amounts NiO-doped cubic *Pm3n* mesoporous silica monoliths (HOM-9) via simple and reproducible one-step synthetic route in which instantly preformed liquid crystalline phase of Brij 56 ($C_{16}EO_{10}$) was adopted [22]. Potential advantages of this strategy are the control of mesopore sizes and shapes, molecular scale homogeneity of NiO-doped silica monoliths, and fast processing synthesis at low temperatures without trailing in the ordered structures.

Due to nickel is inexpensive and well dispersed into the solid supports, considerable attention has been devoted to use the NiO-doped mesoporous materials as effective catalysts in various reactions [15–19]. The increase of the NiO activity might be due to the large surface areas and pore volumes, and uniform porosity at nanometer scale of the mesoporous supports [1–3]. With increasing concern for public health and environmental quality, it is imperative for the complete removal of the organic pollutants from the environment. One of the most commonly used refinery techniques is the chemical transformation of these pollutants to safe hands of compounds. However, the oxidation of organic pollutants such as aminophenols (AP) is very important to produce the phenoxazone compounds, namely, questiomycin A, which is related to naturally antineoplastic agent actinomycin D. The latter is used clinically for the treatment of certain types of cancer [23,24].

Here, we examined the NiO-doped cubic *Pm3n* silica monoliths (HOM-9) as an effective catalyst in the chemical transformation of aminophenols to phenoxazone compounds via a heterogeneous oxidation reaction in aqueous solution. The catalytic reaction studies indicated that the ordered cage NiO/HOM-9 catalyst with uniformly sized pore, high surface area and pore volumes led to homogenous diffusion and fast transport of aminophenol molecules onto the ordered pore networks and active functional sites without large kinetic hindrances, as evidenced from the high degree of conversion and reaction rate. Results show that the reactivity of the oxidation reaction of *o*-AP by NiO/HOM-9 monolithic catalyst was enhanced with high degree of content and dispersion of NiO particles into the mesopore surfaces. Key to our development of the cage NiO/HOM-9 catalysts is that the amorphous catalysts lost about 12% of its original efficiency after a single regeneration/reuse cycle, whereas the ordered monolithic catalysts lost about 6% after five reuse cycles, indicating the long-term activity of the ordered NiO/HOM-9 as a recyclable catalyst.

2. Experiments

2.1. Chemicals

All materials were analytical grade and used as purchased without further purification. Tetramethylorthosilicate (TMOS), nickel nitrate hexahydrate ($Ni(NO_3)_2{\cdot}6H_2O$), nickel chloride hexahydrate ($Ni(Cl)_2{\cdot}6H_2O$), *o*-aminophenol ($C_6H_4OHNH_2$), amorphous silica, and [polyoxyethylene(10) cetyl ether] Brij 56 surfactant, $C_{16}H_{33}(OCH_2CH_2)_{10}OH$ designated $C_{16}EO_{10}$, were purchased from Sigma–Aldrich Company Ltd. (USA). The *o*-AP solution (0.01 mol/L) was prepared in water 3% ethanol (v/v) mixture. However, the percentage of ethanol content is lesser than 0.15% in the *o*-AP solution (5×10^{-4} mol/L) during the oxidation reaction process.

2.2. Synthesis of NiO-doped cubic Pm3n silica monoliths NiO/HOM-9

In general, cubic *Pm3n* mesoporous NiO-silica monoliths (NiO/HOM-9) were fabricated by using microemulsion phases of Brij 56 ($C_{16}EO_{10}$) surfactant as templates in an instantly direct templating method, as previously reported [22]. This fabrication procedure involved the addition of TMOS to Brij 56/C_{12}-alkane (dodecane) mixture to obtain well-homogenized sol–gel, continuous stirring and agitation at 50 °C by using a water bath for approximately ~1 min was necessary. Various amounts of hydrated nickel nitrate, which was completely dissolved in an acidified aqueous solution (HCl/H_2O at pH 1.3), were added to the mixture domains (Brij 56/dodecane/TMOS) to quickly obtain the desired cubic *Pm3n* liquid crystal phase and to initiate the polymerization of the inorganic precursors around this phase assembly. In this systematic design, the microemulsion phase was formulated by mixing C_{12}-alkane (dodecane) to Brij 56 prior to the addition of the TMOS (Brij 56/TMOS mass ratio of 35 wt%) to form a quaternary system (Brij 56:dodecane:TMOS:H_2O). The amount ratio of Brij 56 to dodecane was 2:1 to optimize both the swelling and the interfacial surface curvature of the Brij 56 micelles [22]. The typical synthesis of Ni/HOM-9 monoliths at a specific Brij 56/TMOS mass ratio of 35 wt% in microemulsion system was as follows. First, 0.7 g of Brij 56, 0.35 g dodecane and 2 g TMOS were dissolved in a flask by agitation in a water bath (50 °C) for 1–2 min, yielding a clear solution (i.e., homogenous). To this sol–gel solution, a mixture of *x* g $Ni(NO_3)_2$ (*x* depends upon the Ni content in sample) dissolved in 1 g of H_2O/HCl was quickly added. The mass ratio of Brij 56:TMOS:$Ni(NO_3)_2$:H_2O/HCl was 0.7:0.35:2:*x*:1. In all syntheses, the composition mixture

domains were not aged (i.e., without static condition). However, the exothermic hydrolysis and condensation of TMOS occurred rapidly by addition of HCl/$Ni(NO_3)_2$ to the Brij 56/C_{12}-alkane/TMOS mixture. The methanol produced from the hydrolysis reactions of TMOS at the first stage of the synthesis helps clarify to yield well-homogenized phase domains. To avoid the effect of the destruction of the liquid crystalline phase within the continuous hydrolysis/condensation reaction of TMOS, the removal of methanol was necessary by using a diaphragm vacuum pump (DIVAC 1.2 L) connected with a rotary evaporator at 45 °C. Within ~5–10 min, the resulting green gel-like material acquired the shape and size of the reaction vessel. To obtain macroscopic, crack-free, and shape-controlled translucent and opaque Ni-silica monoliths at centimeter dimension, the gentle drying of the resultant cubic *Pm3n* mesophase monoliths was necessary at room temperature for 3 h and then allowed to stand in a sealed container at 40 °C for 10 h to complete the drying process. The Brij 56 and C_{12}-alkane were removed by calcination at 450 °C (1 h under nitrogen and then 6 h under oxygen).

2.3. Synthesis of amorphous pure NiO catalyst

Large particle sizes and macro-scale length of amorphous NiO (pure) could be fabricated by applying sol–gel process of bulk lyotropic composition mixtures of Brij 56 ($C_{16}EO_{10}$)/$NiCl_2$/acidic H_2O (at pH 1.3). This fabrication procedure involved the addition of ethanol solution of 1 M $NiCl_2$ salt as an inorganic precursor to 4g Brij 56. To obtain well-homogenized sol–gel, continuous stirring and agitation at 50 °C was necessary by using a water bath for approximately ~1 min. A 4 g acidified H_2O was added to the sol–gel composition to induce the interaction between the $NiCl_2$ precursors with (EO-block) of Brij 56. Green gel-like materials were formed when the ethanol was removed by using a diaphragm vacuum pump (DIVAC 1.2 L) connected with a rotary evaporator at 60 °C. At the initial reaction time, the resulting green gel-like material acquired the shape and size of the reaction vessel. Within the extended reaction time or even under dryness at 35–45 °C, the solid co-precipitated in the bottom of the flask, losing the shape-controlled monoliths. The gel-solid materials were dried for several days to complete drying process and the aging of the particle sizes. The Brij 56 surfactant was removed by calcination at 450 °C (1 h under nitrogen and then 6 h under oxygen). Note: in both as-made and calcined materials, the samples were amorphous according to the XRD and N_2 isotherms studies (data not shown).

2.4. Fabrication of NiO-supported amorphous silicas

A direct graphing of 1 M $NiCl_2 \cdot 6H_2O$ into commercially available and amorphous silica was carried out under stirring for several days (~7 days). The supported solid was collected by suction and washed with deionized water. The Ni(II)-supported silica was sealed in the oven at 45 °C for several hours to complete the dryness. The Ni(II)-supported silica was calcined under oxygen for 6 h. The Si/Ni amount ratio was found to be 4, as estimated form the EDX elemental analysis.

2.5. Characterization of amorphous and ordered catalysts

The textural surface properties of the amorphous and ordered catalysts including the specific surface area and the pore structure were determined by N_2 adsorption–desorption isotherms at 77 K with a BELSORP36 analyzer (JP. BEL Co. Ltd). Specific surface area (S_{BET}) was calculated using multi-point adsorption data from linear segment of the N_2 adsorption isotherms using Brunauer–Emmett–Teller (BET) theory. The pore size distribution was then determined from the adsorption curve of the isotherms by using the nonlocal density functional theory (NLDFT). Before the N_2 isothermal analysis, all samples were pre-treated at 300 °C for 8 h under vacuum until the pressure was equilibrated to 10^{-3} Torr. Small- and wide-angle powder X-ray diffraction (XRD) patterns were measured by using an MXP 18 diffractometer (Mac Science Co. Ltd.) with monochromated Cu Kα radiation. Transmission electron microscopy (TEM) samples were prepared by dispersing the powder particles onto holey carbon film on copper grids then TEM micrographs were obtained by using a JEOL "JEM-2000EXII" operating at 200 kV with a side-mounted CCD Camera "Mega View III" (Soft Imaging System Co.). Field emission-scanning electron microscopy (FE-SEM) micrographs were obtained by using a Hitachi S-800 SEM operated at 20 keV. X-ray photoelectron spectroscopy (XPS) was obtained by using a PHI Model 5600 Multi-Technique systems (PerkinElmer Co., USA) with monochromated Al Kα radiation. Energy dispersive X-ray (EDX) micro-analyzers were recorded by using Horiba EMAX Energy EX-320 on Hitachi FE-SEM S-800. The absorbance spectrum of the oxidation product was recorded using UV–vis spectrometer (Shimadzu 3150, Japan).

2.6. Heterogeneous catalytic studies

The heterogeneous oxidation reaction of *o*-AP using ordered NiO/HOM-9 monoliths, amorphous pure NiO, and amorphous NiO-supported silicas as catalysts was carried out at four temperatures (range 30–45 °C) in aqueous solution. The reaction was performed using a thermostatted shaker, where the rate of shaking was kept constant. After a set interval of time, the container was removed from the thermostat and the reaction was quenched quickly by suction or filtration in the case of using monolith or powder catalysts, respectively. Due to the NiO/HOM monolithic features, no filtrated or centrifuging systems were used for detection process, indicating easy kinetic studies [25]. However, in the case of powder catalyst, filtration is the best manifest to control the quenching. The oxidation product of the *o*-AP in heterogeneous systems was monitored spectrophotometrically at 435 nm.

3. Results and discussion

3.1. Simple strategy for synthesis of cage NiO-silica composites

In this synthetic manipulation, well-dispersed and ordered NiO-doped cubic *Pm3n* silica monoliths (NiO/HOM-9) could

be fabricated by using simple, fast (~5 min), and single-step strategy in which instant preformed microemulsion crystalline phase of Brij 56 was used as structure-directing agents. Despite the high Ni contents (Si/Ni = 1) used in the composition mixtures, no changes in the cubic *Pm3n* (HOM-9) phase structures were evident by using this synthesis approach [22], indicating the significant control over the phase domains. However, the addition of C_{12}-alkane, in principle, led to change in the interfacial curvature of Brij 56 ($C_{16}EO_{10}$), thus inducing the phase transition (cubic *Im3m*–cubic *Pm3n*) and swelling the micelle, as exclusively discussed in our previous report [22]. The practical finding here indicated that the addition of nickel precursor to phase composition might act as a secondary oligomer with TMOS and a condensation catalyst, as practically evidenced from the increase of the rate of the polymerization of the TMOS around the phase assembly. However, the Ni(II) oligomer might interact with the hydrophilic (EO) units of Brij-surfactant ($C_{16}EO_{10}$) in the bulk microemulsion phases during the formation of the silica network matrices and thus led to well-distributed Ni(II) ions among the formation of the silica matrices [20].

3.2. Characterization of NiO/HOM-9 monoliths

3.2.1. Small-angle XRD studies

The small-angle XRD patterns of NiO/HOM-9 monoliths (Fig. 1) show well-resolved Bragg peaks that were characteristic of highly ordered cubic *Pm3n* phase domains. Our results significantly show that a unique signal at low 2θ angle ($\leq 1^\circ$), which can be assigned to (1 1 0) refraction. In addition, three well-resolved and high intense peaks in the range of $1.2 \leq 2\theta \leq 1.8^\circ$ assigned to (2 0 0), (2 1 0), and (2 1 1) diffractions were clearly observed even with monoliths containing high amounts of Ni at Si/Ni = 1 [26], indicating the formation of ordered cubic structure with *Pm3n* space group. Although the structural ordering was evident with low silica contents of monoliths, the broadening and low resolution of the low intensity peaks in the region $2 \leq 2\theta \leq 4^\circ$ (Fig. 1(e) and (d)) indicated the formation of the short range ordering of NiO/HOM-9 monoliths. In addition, the increase in the cubic *Pm3n* lattice constants ($a = d_{210}\sqrt{5}$) with increasing the Ni contents (Table 1), possibly due to the incorporation of the Ni (II) ions into the pore frameworks might lead to longer Si–O–Ni bond length compared to the Si–O–Si bond.

3.2.2. Wide-angle XRD studies

The wide-angle XRD patterns of calcined NiO/HOM-9 monoliths (Fig. 2) show several diffraction peaks assigning to the (1 1 1), (2 0 0), (2 2 0), (3 1 1), (2 2 2) plans for pure face-centered cubic (fcc) NiO nanocrystals with lattice constants of a = 0.41 nm [27]. Based on the line width of the (1 1 1) diffraction plane, the crystallite particle size of NiO was determined by using Scherrer formula, $t = 0.91\lambda/(B\cos\theta)$, where t is the crystallite size, λ is the incident radiation wavelength, θ is the Bragg angle, and B is the full-width at half maximum of the diffraction peak. Fig. 2 shows that the well-resolved NiO peaks become more sharp and intense with increasing Ni contents into HOM-9 monoliths, indicating the fabrication of large NiO crystallite particles (>10 nm) (see Table 1). With low NiO-doped silica cubic *Pm3n* monoliths (Si/Ni < 9), the diffraction peaks of NiO particles were broaden [19,20,28], suggesting small crystallite particle size (Table 1) and low crystallinity. Such small NiO crystallite particles might

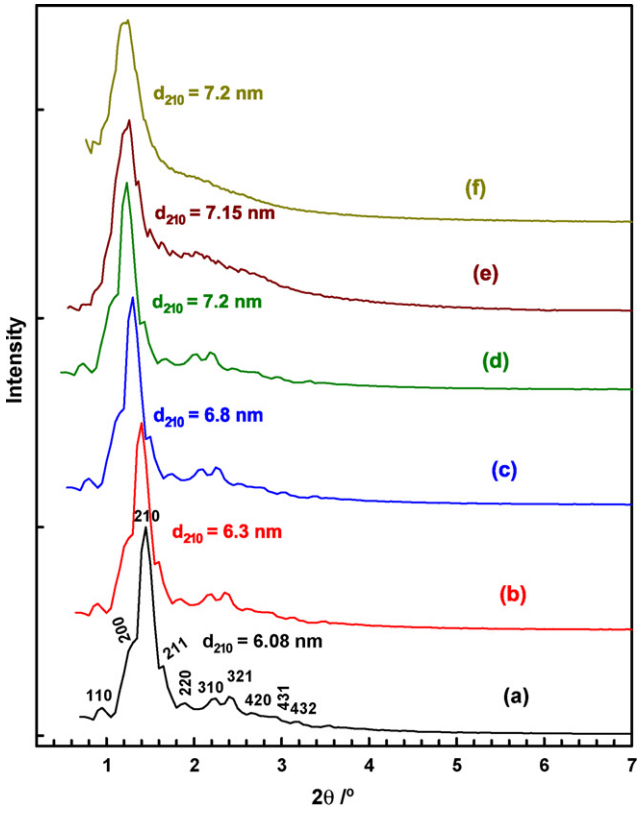

Fig. 1. Small-angle XRD patterns of calcined cubic *Pm3n* mesoporous silica monoliths (HOM-9) with different amounts of NiO nanoparticles with the Si/Ni molar ratio of (a) 0, (b) 19, (c) 9, (d) 4, (e) 1.5, and (f) 1, respectively.

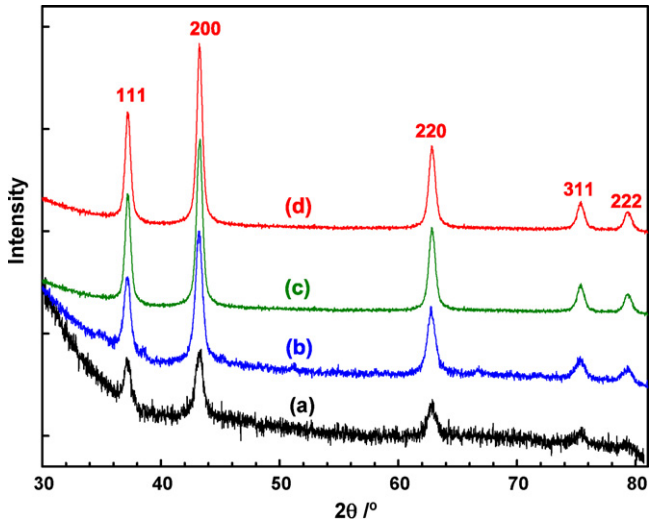

Fig. 2. Wide-angle XRD patterns of calcined cubic *Pm3n* mesoporous silica monoliths (HOM-9) with different amounts of NiO nanoparticles with the Si/Ni molar ratios of (a) 19, (b) 9, (c) 4, and (d) 1.5, respectively.

Table 1
Texture parameters of the catalysts including cubic *Pm3n* NiO/HOM-9 monoliths synthesized in microemulsion mesophase of Brij 56 surfactant at Brij 56/TMOS ratios of 35 wt%, amorphous NiO and amorphous NiO-supported silica; mesopore volume (V_p), unit lattice dimension (α_o), BET surface area (S_{BET}), pore size (R_{Cav}), wall thickness (W), and the NiO crystallite size (Cz)

Catalysts	α_o (nm)	S_{BET} (m^2/g)	V_P (cm^3/g)	R_{cav} (nm)	W (nm)	Cz (nm)
HOM-9	13.6	700	0.72	4.4	9.2	–
NiO/HOM-9 (19)	14.1	755	0.66	4.3	9.8	6.0
NiO/HOM-9 (9)	15.2	734	0.69	4.5	10.7	7.5
NiO/HOM-9 (4)	16.2	698	0.68	4.7	11.5	10
NiO/HOM-9 (1.5)	16.0	634	0.69	4.6	11.4	12
NiO/HOM-9 (1)	16.0	600	0.69	4.6	11.4	14
Amorphous NiO	0.41	124	0.15	160	–	20
Amorphous NiO-SiO_2 (4)	0.42	50	0.12	–	–	21

be partially wrapped into the pore surfaces of the cage cubic *Pm3n* monoliths. However, in general, the large particle size of NiO could not be wrapped inside the cavity of the cage pores, as evidenced from the TEM profile and N_2 isotherms.

3.2.3. TEM micrographs for cubic Pm3n NiO-silica nanostructures

TEM images revealed regular arrays running along a large area of all directions, particularly with samples containing low Ni contents of Si/Ni ratios $\leq$4 (Fig. 3a–d). The well-defined white dots-like pores along the channels confirmed the high degree of 3D architecture ordering, as consistent with the reported mesoporous SBA-1 and SBA-6 of cubic *Pm3n* phase [29,30]. Although, the formation of worm-like mesopores in large domains (Fig. 3e and f) was revealed with the high Ni contents (Si/Ni $\geq$ 1.5), still ordered pores connected in channels were characteristics these monolithic samples. Results here, in general, indicated the retention of the ordered structures of cubic *Pm3n* lattice even with high doping of NiO particles, as consistent with XRD patterns (Fig. 1). TEM micrographs also show that the dark dots with irregular sizes were dispersed on the patterns, indicating that the NiO nanoparticles might diffuse into the mesochannel pores. In addition, the NiO nanoparticles underwent the aggregation, and therefore led to anisotropic growth to larger crystallite sizes, particularly with samples containing low Si/Ni ratios (Fig. 3e and f). This finding indicated that by using our synthetic strategy, the NiO species might be embedded on the external surface of the silica-host matrices with difficulty to entrap or organize into the inner pore surfaces of the cage cubic *Pm3n* structures, as evidenced from the large NiO crystallite particle sizes (Table 1).

3.2.4. Morphology and dispersion of NiO-silica composites

SEM micrograph (Fig. 4(A)) revealed that the NiO/HOM-9 monoliths had a large particle sizes (50–150 μm in diameter). In general, the crystal particles of these monoliths (as-made and

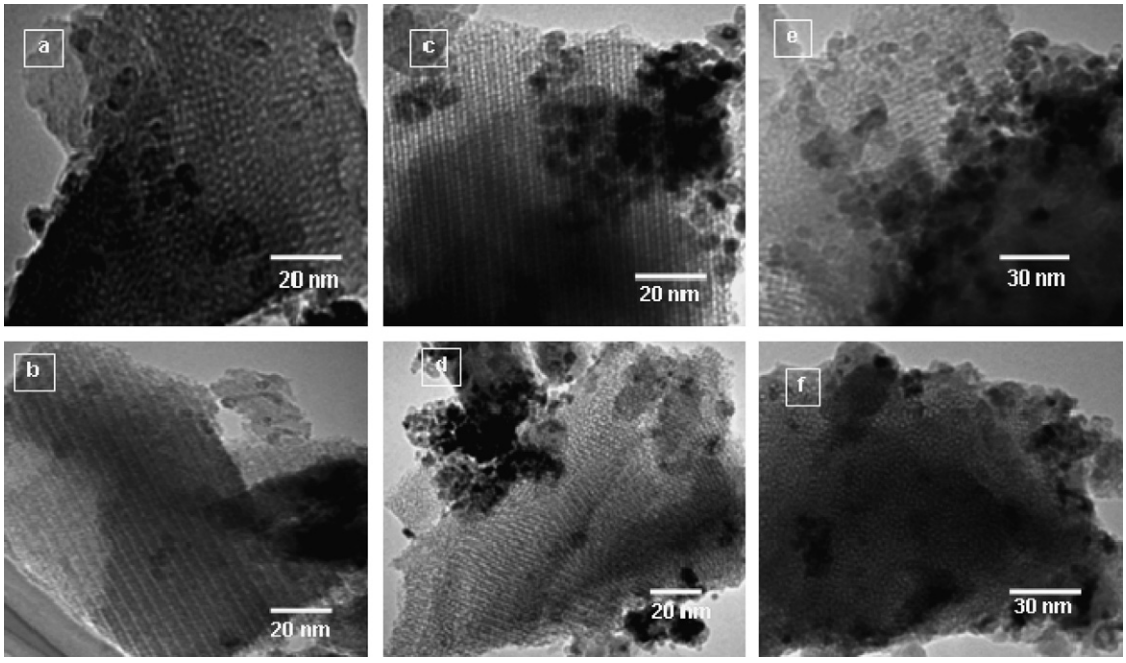

Fig. 3. Representative TEM images of cubic *Pm3n* mesoporous silica monoliths (HOM-9) with different amounts of NiO nanoparticles recorded along the (a) [2 1 0], and (b) [1 1 0] directions for NiO/HOM-9 (19) sample, and the (c) [1 0 0], (d) [1 1 1] zone axes of NiO/HOM-9 (9) and (4) samples, respectively. Worm-like mesopore NiO/HOM-9 monoliths fabricated at the Si/Ni molar ratios of (e) 1.5, and (f) 1, respectively.

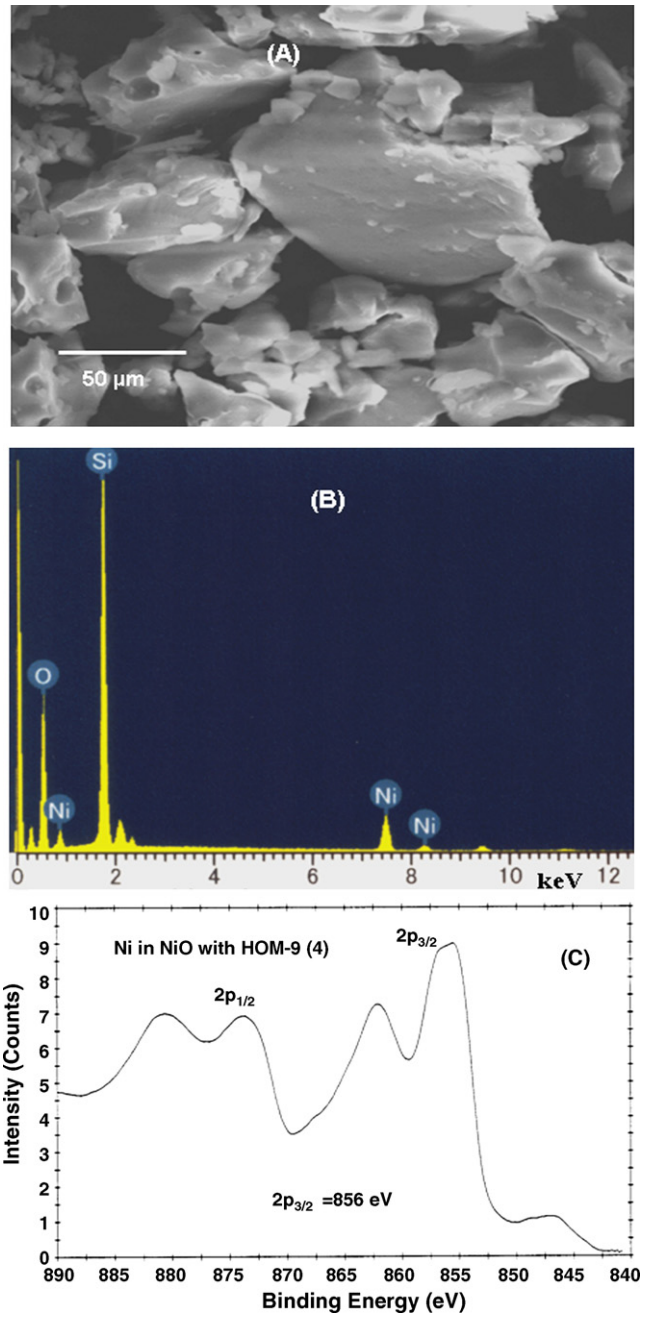

Fig. 4. FE-SEM image (A), the corresponding EDX spectrum (B), and XPS pattern of the Ni 2p for NiO-doped into cubic *Pm3n* mesoporous silica monoliths (NiO/HOM-9) with the Si/Ni molar ratios of 4.

calcined forms) were predominantly platelet-like morphology with fine smooth surfaces similar to the HOM-9 silica monoliths [22,26]. SEM patterns (all data not shown) indicated that no morphological transition was evident even with high doping NiO species into the monoliths. EDX technique provided evidence of the NiO/HOM-9 composition; however, the spectrum (Fig. 4B) was recorded over wide-range domains and on several spots. Overall, the EDX analyses revealed that the Si/Ni values were compatibly averaged with the bulk quantities of synthesized NiO-HOM-9 samples regardless the self-aggregation of NiO species, as shown in TEM profiles

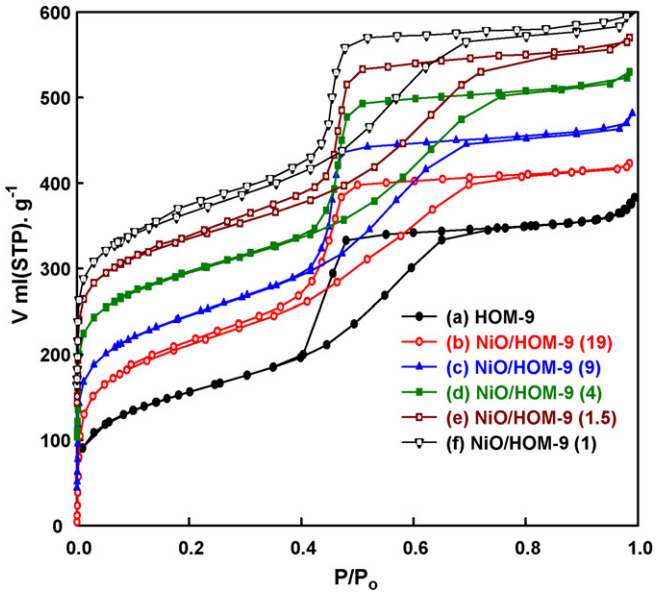

Fig. 5. Nitrogen adsorption–desorption isotherms of cubic *Pm3n* mesoporous silica monoliths (HOM-9) with different amounts of NiO nanoparticles with the Si/Ni molar ratio of (a) 0, (b) 19, (c) 9, (d) 4, (e) 1.5, and (f) 1, respectively. Isotherms (c), (d), (e), and (f) were shifted vertically by 30, 90, 130, and 150 ml (STP) g^{-1}, respectively.

(Fig. 3c–f). This finding indicates the homogeneous dispersion, to some extent, of the NiO particles over the monoliths.

The XPS pattern of Ni 2p spectra (Fig. 4C) shows two edges of $2p_{1/2}$ (~870–885 eV) and $2p_{3/2}$ (~850–865 eV), respectively. The XPS spectra of NiO-HOM-9 catalyst show two main peaks of $2p_{1/2}$ and $2p_{3/2}$ at 856.4 and 874.3 eV, which assigned to the Ni(II) ion in the NiO particles. In turn, the binding energy of Ni $2p_{3/2}$ peak was shifted around 2.0 eV to higher values compared to that of pure NiO (854.4 eV) with higher proportions of Ni(II) ions in the oxide form than that in the spinal form. This blue shift in the $2p_{3/2}$ peak could be assigned to the existence of the small particles of NiO inside the HOM mesopores [17]. The XPS results, in general, were mainly indicated the dispersion of the dominant Ni(II) ions in intrinsic NiO particles into the pore wall surfaces of HOM silicas [31].

3.2.5. N_2 isotherms of cage-like pore NiO-silica composites

N_2 isotherms (Fig. 5) show that the NiO/HOM-9 mesoporous monoliths exhibited typical reversible type-IV adsorption isotherms with H_2 hysteresis loops. These loops are characteristics of uniform cage mesoporous materials [32–34]. The isothermal shape significantly indicated that with doping high NiO contents, the position of the capillary condensation step gradually shifted to higher relative pressure. This shift revealed a systematic increase in cavity size (Table 1). Practically important issue was the retention of the cage character even with doping high NiO contents (Fig. 5e and f). This finding mainly indicated that most of the large NiO particles were located into the external pore surfaces. In addition there is no blocking of the inner pores from the doping of such large particle sizes of NiO, as evidenced for the slight decrease of

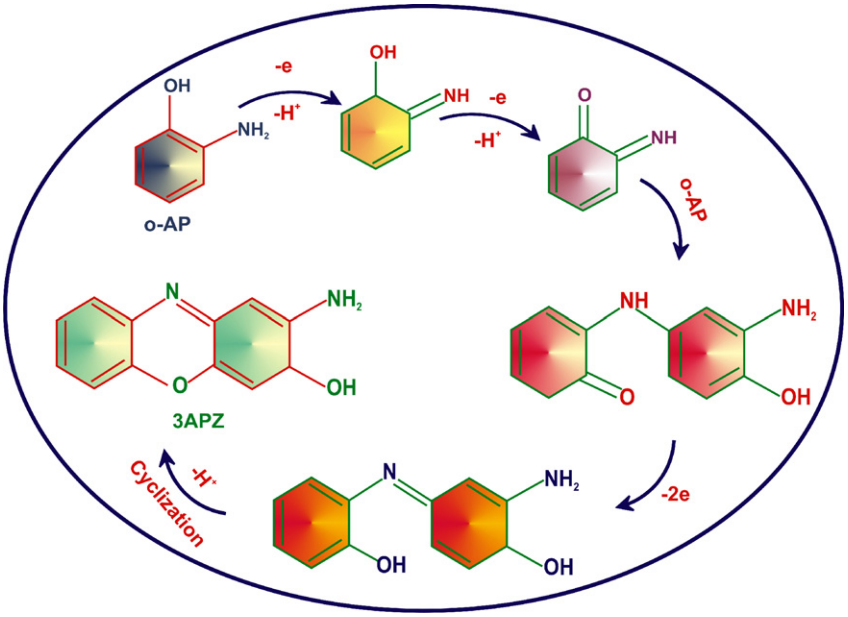

Scheme 1. Mechanistic formation of 2-aminophenoxazine-3-ol (3APZ) through the oxidative condensation process involves a $4e^-$ oxidation for *o*-AP by using NiO catalysts.

pore volume and increase in the surface area (Table 1). However, the higher surface area with doping NiO species assigned the high degree of dispersion on the outer surfaces. Although the location of large NiO crystallite size species in the outer pore surfaces might lead to difficult control over the NiO crystallite sizes and over the degree of aggregations, the regularity and the catalytic properties (see below) of the catalyst monoliths were substantially enhanced with larger amount of doped NiO, uniform pore size, high surface area and large pore volumes [15].

3.3. Catalytic oxidation of aminophenol

To investigate the applicability of the cage NiO/HOM-9 monoliths as catalysts, the heterogeneous oxidation of *o*-AP was carried out by using amorphous pure NiO, NiO-supported amorphous silicas, and the cage NiO/HOM-9 materials. The oxidation of *o*-AP by using catalysts in an aqueous solution (Scheme 1) led to the formation of 3-aminophenoxazone (3-APZ) compound, as previously reported [25,35]. Moreover, the oxidation product (3-APZ) was analyzed by CHNO elemental analyses. The data were as follows: C, 66.97; H, 4.7; N, 13.0, and O, 15.0 as consistent with $C_{12}H_{11}O_2N_2$ molecular formula, which requires C, 67.2; H, 4.67; N, 13.08, and O, 14.95%. The 3-APZ product was received a great attention in the promising treatments for cancer [23,24]. The oxidative condensation process over NiO-supported catalysts involved a $4e^-$ oxidation for *o*-AP to produce 2-aminophenoxazine-3-ol (3APZ) (Scheme 1). Generally, the first $2e^-$ oxidation is a result of the reduction of the NiO particles [35]. This means that two equivalents of the metal oxides are initially reduced by one equivalent of the *o*-AP molecule. Since the benzoquinone imines react with another molecule of the *o*-AP to afford the dimeric oxidation products, the reaction sequence of the expected oxidation products is shown in Scheme 1.

3.3.1. Control batch contact-time experiments

The kinetic responses of the formation of 3-APZ oxidation product were studied by continuously monitoring the UV–vis absorption at $\lambda = 435$ nm as a function of time, as shown in Fig. 6. In addition, the oxidation rate of *o*-AP on the amorphous NiO particles or mesoporous NiO/HOM-9 monoliths was increased as a function of the temperature (Fig. 7), which is considered to be one of preferable key clues of the reaction activity. However, the increase in solution temperature of *o*-AP [5×10^{-4} M] had significant influence on the rate of catalysts. Temperature-dependent kinetic responses were monitored by the absorption signal of 3-APZ (Fig. 7). Result suggests that the *o*-AP molecule-diffusion was enhanced by using NiO catalysts

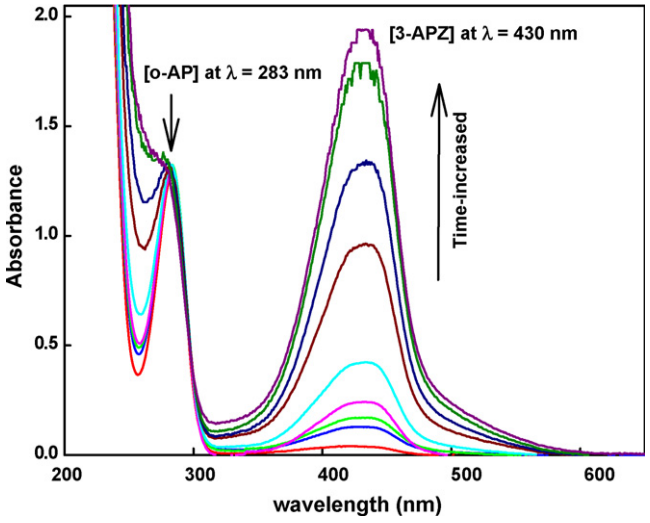

Fig. 6. Time-sequence of the increase the absorption band of 3-APZ at 430 nm during the catalytic reaction of *o*-AP [5×10^{-4} M] on the cubic *Pm3n* mesoporous NiO-silica monoliths (NiO/HOM-9) with the Si/Ni molar ratios of 4 at 40 °C.

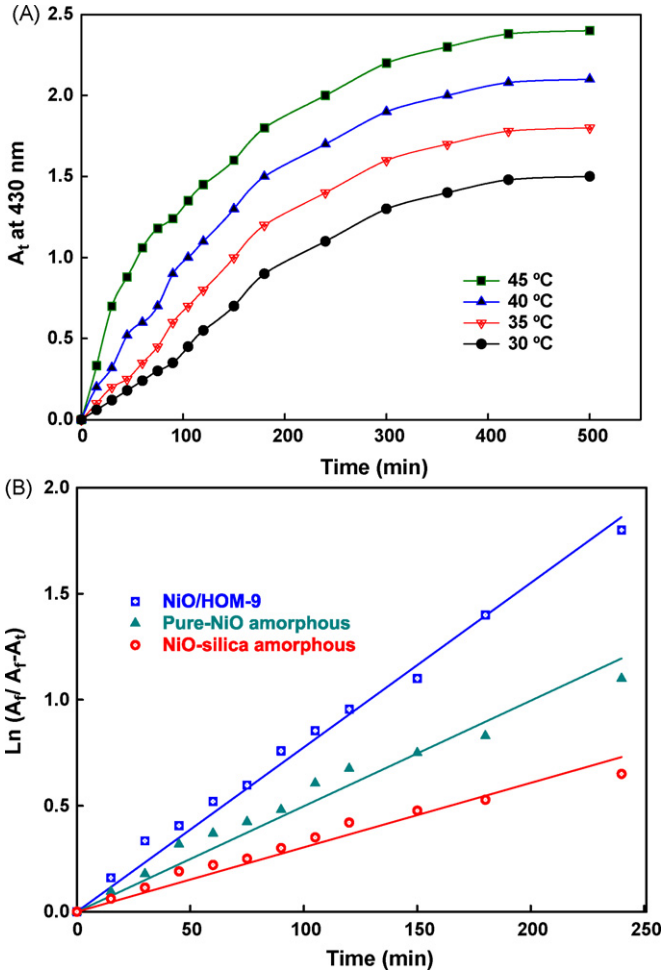

Fig. 7. (A) Effect of various reaction temperatures on the time-rate dependence of the formation of 3-APZ compound during the catalytic reaction of *o*-AP [5×10^{-4} M] on the cubic *Pm*3*n* mesoporous NiO-silica monoliths (NiO/HOM-9) with the Si/Ni molar ratios of 4. (B) Integrated first-order reaction rate of the [5×10^{-4} M] *o*-AP oxidation reaction by using NiO catalysts with ordered cage NiO-HOM-9 with Si/Ni molar ratios of 4 (a), amorphous NiO (b), and amorphous NiO-supported silica with Si/Ni molar ratios of 4 (c) at 45 °C for 2 h.

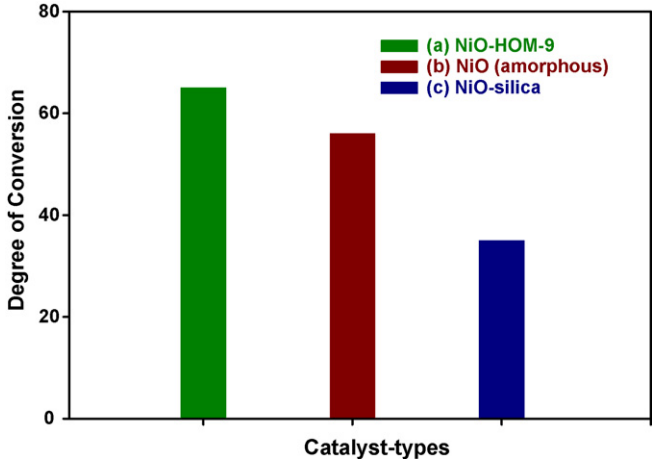

Fig. 8. The degree of conversion of 3-APZ compound during the oxidation of *o*-AP [5×10^{-4} M] by using NiO catalysts with ordered cage NiO-HOM-9 with Si/Ni molar ratios of 4 (a), amorphous NiO (b), and amorphous NiO-supported silica with Si/Ni molar ratios of 4 (c) at 45 °C for 2 h.

at high temperatures, as evidenced from the increase of the reaction rate (Table 2). The increase in the reaction temperature led to enhance the internal energy of the *o*-AP aqueous phase and to facilitate the mass transfer through the NiO clusters with high molecule-percolation. The latter behavior might also be responsible for the comparative decrease in the hindrance effect of *o*-AP over the catalysts (Table 2). The reaction rate of the *o*-AP oxidation was analyzed according to the first-order kinetic equation, as consistent with previous studies (Fig. 7B) [25,36]:

$$\ln\left(\frac{A_f}{A_f - A_t}\right) = k\,m\,t \quad (1)$$

where, A_f is the absorbance of 3-APZ at infinite time, A_t is the absorbance of 3-APZ at time (t), k is the first-order reaction constant (s^{-1}), and m (g) is the amount of catalysts. It is well known that the rate constant (k), which is only temperature dependent, is determined from the slope of the linear first-order kinetic equation (Table 2). Results (Fig. 7B) show evidence that

Table 2
Catalytic activity, the fractions of *o*-AP covered surface catalysts (f_c), and the catalytic efficiency of after several regeneration/reuse cycles of the NiO catalysts during the oxidation reaction of *o*-AP [5×10^{-4} M] onto the uniformly sized cage cubic *Pm*3*n* NiO-silica mesopore monolithic (NiO/HOM-9) with various Si/Ni molar ratios, amorphous NiO, and amorphous NiO-supported silica with Si/Ni molar ratios of 4 at various temperature ranges

Catalysts	f_c (g/m^2)	$10^4\,k_t$ (s^{-1}) at T °C				Catalyst reusability			
		30	35	40	45	f_c (g/m^2)	E (%) at cycle no.		
							1	3	5
HOM-9	1.7	–	–	–	–[a]	–	–	–	–
NiO/HOM-9 (19)	6.02	0.24	0.34	0.49	0.85	5.9	99	97	96
NiO/HOM-9 (9)	8.3	0.51	0.73	1.05	1.8	8.2	99	98	96
NiO/HOM-9 (4)	10.3	1.13	1.64	2.4	4.04	10.1	98	96	95
NiO/HOM-9 (1.5)	12.2	3.04	4.37	6.3	10.8	12.0	97	96	94
NiO/HOM-9 (1)	14.0	4.59	6.56	9.3	16.1	13.8	97	96	94
Amorphous NiO	9.5	0.95	1.38	2.01	3.37	9.0	90	87	85
Amorphous NiO-SiO_2 (4)	8.1	0.60	0.87	1.27	2.14	7.5	88	85	84

[a] The HOM-9 silica is catalytically inert towards the oxidation of *o*-AP molecule.

the first-order reaction rate is controlled the *o*-AP oxidation reaction.

3.3.2. Efficiency of the ordered catalysts

Our experimental results show that the NiO-doped cage HOM-9 monoliths exhibited higher reaction activity than that of amorphous NiO or NiO-supported silica materials (Fig. 8). Results indicated that the open, uniform pore-cage architectures, high surface area and large pore volumes allowed efficient adsorption and diffusion of *o*-AP [5×10^{-4} M] to the active site of NiO clusters. The high mass-transport and the adsorption were significantly affected by the 3D pore geometry and shape, as evidenced from the f_c value of the catalysts (Table 2). However, the fractions of the coverage surfaces (f_c) occupied by the *o*-AP molecule, which expressed the extent of *o*-AP adsorption per unit area of catalysts, are calculated according the following equation [37].

$$f_s = \frac{M\beta}{S}\ (\mathrm{mg/m^2}) \qquad (2)$$

where, M is the molecular area of *o*-AP, β is the number of *o*-AP molecules adsorbed per unit area of catalysts, and S is the surface area of catalysts. The calculated f_c values revealed that the mass-diffusion effectively appended to the ordered nanoscale structures, as evidenced by the higher f_c value of ordered cage NiO-HOM-9 catalysts compared to amorphous NiO or NiO-supported silica catalysts (Table 2) [37]. The difference in the diffusive mass transport behavior of these catalysts reveals the significant effect of uniformly sized pore, high surface area and pore volumes on homogenous diffusion and fast transport of *o*-AP molecules onto the ordered networks and active functional sites without large kinetic hindrances (Scheme 2). Results, in general, indicated that ordered nanoscale pore geometry plays a role in the design of efficient catalysts that might be effective for various heterogeneous reactions.

3.3.3. Effect of the Ni/Si contents on the reaction activity

Batch contact-time experiments show that oxidation activity of *o*-AP [5×10^{-4} M] was substantially influenced by the amount of NiO-doped the HOM-9 monoliths (Fig. 9). However, the reaction activity was increased with high NiO-doped the cage monoliths, despite the location of the NiO particles inside or outside the pore cavity frameworks. Figure 9 revealed that the high accessibility and mobility of the small molecular size such as *o*-AP (~6 Å) crucially affected by the degree of the uniformity, regularity of the mesopore and the amount of the functional sites. This finding also indicated that the well-dispersed NiO nanoparticles into the silica matrices played the leading role in the improvements of catalytic reaction [38]. Thus, the dispersion of NiO particles was likely to be homogenous even with monoliths that have large NiO crystallite sizes (≥10) under our synthetic manipulation, as consistent with EDX and TEM profiles.

Interestingly, the extent of *o*-AP adsorption per unit area of NiO/HOM-9 catalysts (f_c) helps clarify that changes in surface

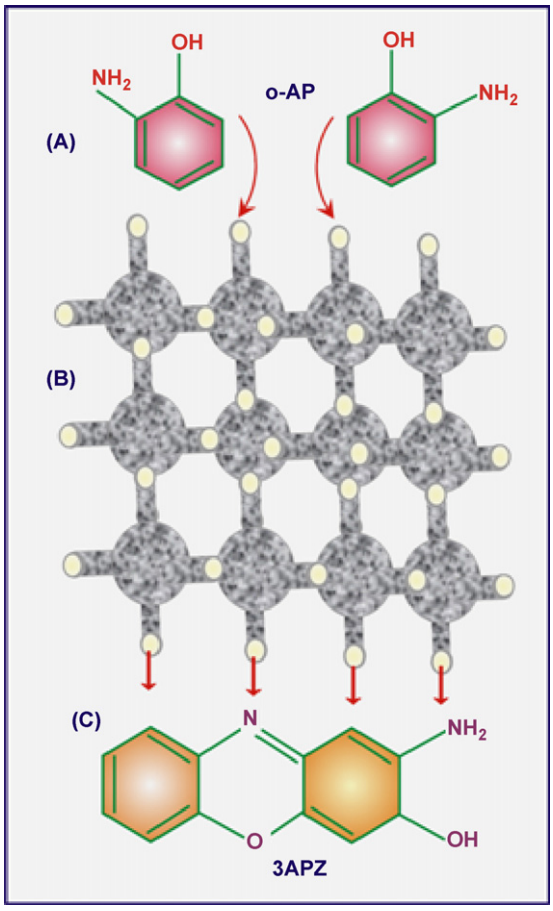

Scheme 2. Systematic representative of the possible accessibility of *o*-AP [5×10^{-4} M] (A) onto the uniformly sized cage cubic *Pm3n* NiO-silica (B) mesopore monolithic (NiO/HOM-9) catalysts during the formation of 3-aminophenoxazone (3-APZ) compound (C).

chemistry of cage silica HOM-9 by impregnation of NiO composites, even with low amounts of Ni/Si ratios, were more important to led the high affinity of the adsorption and accessibility of *o*-AP. In general, the f_c values (Table 2) quantitatively indicated that the NiO-HOM-9 monoliths can act

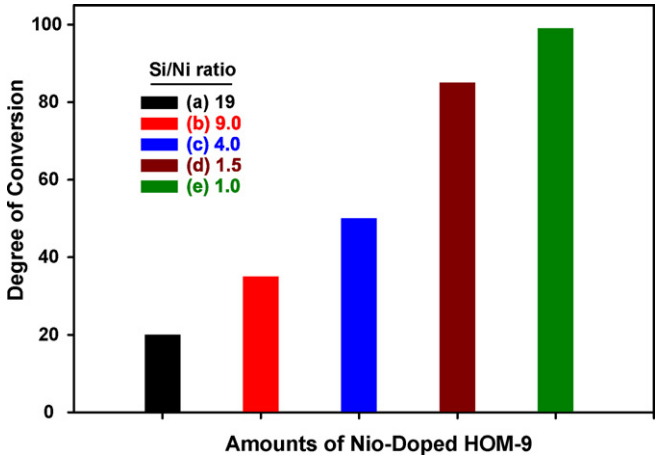

Fig. 9. The degree of conversion of 3-APZ compound by using the cubic *Pm3n* mesoporous NiO-silica monoliths (NiO/HOM-9) as catalysts with the Si/Ni molar ratios of (a) 19, (b) 9, (c) 4, (d) 1.5, and (e) 1, respectively, at 40 °C for 2 h.

as effective catalysts for the oxidation of organic *o*-AP pollutants to hand-safe chemical transformation products.

3.3.4. Reusability of the amorphous and ordered catalysts

One of the most significant issues here is the long-term activity of the ordered NiO/HOM-9 catalysts, despite the reusability in this oxidation reaction. The catalytic stability is of particular interest in developing recyclable catalysts, permitting their important characteristic features and desirability in the industrial applications. After the first set of reaction experiments, the monolith catalyst was collected and washed by slightly acidic aqueous solution (the concentration of HCl = 1×10^{-3} M) for several times and then dried at 200 °C for 12 h under air to remove the 3-APZ adsorbate on the surfaces. The catalytic experiments after several regeneration/reuse cycles of the catalysts show that no significant changes in the adsorption affinity of *o*-AP [5×10^{-4} M] molecule from aqueous solution, as evidenced quantitatively from the f_c values (Table 2), particularly with ordered cage catalysts (NiO/HOM-9). These results clearly indicated that the binding of organic moieties (reactant and product) onto cage catalyst did not lead to the degradation of the internal/external mesopore surface sites, rendering to the facile diffusion and fast particle transport of the molecules to the functional NiO clusters. However, results show that the amorphous catalysts lost about 12% of its original efficiency after a single regeneration/reuse cycle, whereas the ordered monolithic catalysts lost about 6% after five reuse cycles. Clearly evident was that the change in the textural properties of the regenerated NiO/HOM-9 monoliths after releasing the organic moieties was unremarkable (the decrease in parameters was $\leq$2% from the original data, Table 1), indicating the high efficiency in the catalytic reactions. It is also important to note that the shapes and sizes of the NiO/HOM-9 cage cavity were significantly unchanged after several recycles, indicating the retention of cage characters. These results indicated that the ordered NiO/HOM-9 monoliths remained effective even after extended regeneration and recycle use.

4. Conclusion

Well-dispersed and ordered NiO-doped silica monoliths (HOM-type) could be fabricated with cubic *Pm3n* structures by using simple, fast (~5 min), and single-step strategy on which instant preformed microemulsion crystalline phases of Brij 56 was used as structure-directing agents. The small-angle XRD patterns of NiO/HOM-9 monoliths show well-resolved Bragg peaks that were characteristic of highly ordered cubic *Pm3n* phase domains. However, face-centered cubic (fcc) described the NiO nanocrystals with particle sizes of 6–15 nm range. TEM micrographs revealed that the NiO nanoparticles with irregular sizes were doped the pore cavity, particularly with low content of NiO. Results also provide evidence that the retention of the cage character of the mesopore materials was attained even with doping high NiO contents, permitting their desirability in the catalytic reaction. These NiO-silica monoliths can act as an effective catalyst to the formation of biological active phenoxazone compounds that usually used in treatment of certain types of cancer. Among all catalysts used, the ordered cage catalyst with open, uniform pore architectures, high surface area and large pore volumes allowed efficient adsorption and diffusion of aminophenols to the active site of NiO clusters, leading to high degree of conversion and reaction rate. Practically important issue was that the developing recyclable catalysts using NiO/HOM-9 monoliths; however, these catalysts remained their functionalities toward the oxidation of *o*-AP even after extended regeneration and recycle use.

References

[1] M.E. Davis, Nature 417 (2002) 813.
[2] A. Corma, P. Atinzar, H. Garcia, J.-Y. Chane-Ching, Nat. Mater. 3 (2004) 394.
[3] X. He, D. Antonelli, Angew. Chem. Int. Ed. 41 (2002) 214.
[4] A. Corma, Chem. Rev. 97 (1997) 2373.
[5] S.X. Zhao, G.Q. Lu, G.J. Millar, Ind. Eng. Chem. Res. 35 (1996) 2075.
[6] S.A. El-Safty, T. Balaji, H. Matsunaga, T. Hanaoka, F. Mizukami, Angew. Chem. Int. Ed. 45 (2006) 7202.
[7] J.V. Ryan, A.D. Berry, M.L. Anderson, J.W. Long, R.M. Stroud, V.M. Cepak, V.M. Browning, D.R. Rollson, C.I. Merzbacher, Nature 406 (2000) 169.
[8] C.T. Kresge, M.E. Leonowicz, W.J. Roth, J.C. Varttuli, J.S. Beck, Nature 395 (1992) 710.
[9] D. Zhao, J. Feng, Q. Huo, N. Melosh, G.H. Fredrickson, B.F. Chmelka, G.D. Stucky, Science 279 (1998) 548.
[10] P. Yang, D. Zhao, D.I. Margolese, B.F. Chmelka, G.D. Stucky, Nature 396 (1998) 152.
[11] D. Li, H. Zhou, I. Honma, Nat. Mater. 3 (2004) 65.
[12] D. Grosso, C. Boissiere, B. Smarsly, T. Brezesinki, N. Pinna, P.A. Albouy, H. Amenitsch, M. Antonietti, C. Sanchez, Nat. Mater. 3 (2004) 787.
[13] X. Zou, T. Conradsson, M. Klingsted, M.S. Dadachov, M. O'Keeffe, Nature 437 (2005) 716.
[14] J.Y. Ying, C.P. Mehnert, M.S. Wong, Angew. Chem. Int. Ed. 38 (1999) 56.
[15] J. Jia, Y. Wang, E. Tanabe, T. Shishido, K. Takehira, Microporous Mesoporous Mater. 57 (2003) 283.
[16] S.J.S. Basha, N.R. Sasirekha, R. Maheswari, K. Shanthi, Appl. Catal. A 308 (2006) 91.
[17] R. Moreno-Tost, J. Santamaria-González, P. Maireles-Torres, E. Rodríguez-Castellón, A. Jiménez-López, J. Mater. Chem. 12 (2002) 3336.
[18] U. Junges, S. Disser, G. Schimd, F. Schmid, F. Schuth, Stud. Surf. Sci. Catal. 117 (1998) 217.
[19] Y. Park, T. Kang, J. Lee, P. Kim, H. Kim, J. Yi, Catal. Today 97 (2004) 195.
[20] Y. Park, T. Kang, P. Kim, J. Yi, J. Colloid Interface Sci. 295 (2006) 464.
[21] H. Yang, Q. Lu, F. Gao, Q. Shi, Y. Yan, F. Zhang, S. Xie, B. Tu, D. Zhao, Adv. Funct. Mater. 15 (2005) 1377.
[22] S.A. El-Safty, T. Hanaoka, Chem. Mater. 16 (2004) 384.
[23] U. Hollstien, Chem. Rev. 74 (1974) 625.
[24] E. Frei, Cancer Chemother. Rep. 58 (1974) 49.
[25] J. Evans, A.B. Zaki, M.Y. El-Sheikh, S.A. El-Safty, J. Phys. Chem. B 104 (2000) 10271.
[26] S.A. El-Safty, T. Hanaoka, Adv. Mater. 15 (2003) 1893.
[27] X.-M. Liu, X.-G. Zhang, S.-Y. Fu, Mater. Res. Bull. 41 (2006) 620.
[28] D.J. Lensveld, J.G. Mesu, A.J. van Dillen, K.P. de Jong, Microporous Mesoporous Mater. 44 (45) (2001) 401.
[29] Q. Huo, D.I. Margolese, P.Y. Feng, T.E. Gier, G.D. Stucky, R. Leon, P.M. Petroff, U. Ciesla, F. Schüth, Nature 368 (1994) 317.
[30] Y. Sakamoto, M. Kaneda, O. Terasaki, D.Y. Zhao, J.M. Kim, G.D. Stucky, H.J. Shin, R. Ryoo, Nature 408 (2000) 449.
[31] Y. Wang, C. Ma, X. Sun, H. Li, Microporous Mesoporous Mater. 71 (2004) 99.

[32] J.R. Matos, M. Kruk, M. Jaroniec, L. Zhao, T. Kamiyama, O. Terasaki, T.J. Pinnavaia, Y. Liu, J. Am. Chem. Soc. 125 (2003) 821.
[33] B.N. Newalkar, S. Komarneni, U.T. Turaga, H. Katsuki, J. Mater. Chem. 13 (2003) 1710.
[34] S.A. El-Safty, T. Hanaoka, F. Mizukami, Chem. Mater. 17 (2005) 3137.
[35] J. Kaizer, R. Csonka, G. Speier, J. Mol. Catal. A 180 (2002) 91.
[36] J. Bajpai, R. Shrivastava, K. Bajpai, J. Appl. Pol. Sci. 103 (2007) 2581.
[37] S.A. El-Safty, J. Colloid Interface. Sci. 260 (2003) 184.
[38] Y. Takahara, J.N. Kondo, T. Takata, D. Lu, K. Domen, Chem. Mater. 13 (2001) 1194.